



**Ambient Blade Coating of Mixed Cation, Mixed Halide
Perovskites without Drip: In Situ Investigation and Highly
Efficient Solar Cells**

Journal:	<i>Journal of Materials Chemistry A</i>
Manuscript ID	TA-COM-11-2019-012890
Article Type:	Communication
Date Submitted by the Author:	24-Nov-2019
Complete List of Authors:	<p>Tang, Ming-Chun; King Abdullah University of Science and Technology (KAUST), MSE; Fan, Yuanyuan; Shaanxi Normal University Barrit, Dounya; King Abdullah University of Science and Technology, Materials Science and Engineering, Physical Sciences and Engineering Division Chang, Xiaoming; Shaanxi Normal University Dang, Hoang; North Carolina State University, Materials Science and Engineering Li, Ruipeng; Cornell University, CHESS Wang, Kai; King Abdullah University of Science and Technology Smilgies, Detlef; Cornell University, CHESS Liu, Shengzhong; Shaanxi Normal University De Wolf, Stefaan; École Polytechnique Fédérale de Lausanne, Institute of Microengineering – Photovoltaics and Thin Film Electronics Laboratory Anthopoulos, Thomas; King Abdullah University of Science and Technology Physical Sciences and Engineering Division, Materials Science and Engineering Zhao, Kui; Shaanxi Normal University, Key Laboratory of Applied Surface and Colloid Chemistry, MOE, School of Materials Science and Engineering Amassian, Aram; North Carolina State University, Materials Science and Engineering</p>

ARTICLE

Ambient Blade Coating of Mixed Cation, Mixed Halide Perovskites without Drip: *In Situ* Investigation and Highly Efficient Solar Cells

Received 00th January 20xx,
Accepted 00th January 20xx

DOI: 10.1039/x0xx00000x

Ming-Chun Tang^a, Yuanyuan Fan^b, Dounya Barrit^a, Xiaoming Chang^b, Hoang Dang^c, Ruipeng Li^d, Kai Wang^a, Detlef-M. Smilgies^e, Shengzhong (Frank) Liu^b, Stefaan De Wolf^a, Thomas D. Anthopoulos^{a*}, Kui Zhao^{b*}, and Aram Amassian^{a,c*}

Perovskite photovoltaics have made extraordinary strides in efficiency and stability thanks to process and formulation developments like the anti-solvent drip and mixed-cation mixed-halide compositions. Solar cell fabrication through low-cost scalable methods, such as blade coating cannot accommodate the anti-solvent drip and needs to be performed in ambient atmosphere. Consequently, their efficiency has lagged behind that of spin-cast devices, fabricated in inert atmosphere and with carefully timed anti-solvent drip to control nucleation and growth. In this study, we demonstrate formamidinium (FA)-dominated mixed-halide mixed-cation perovskite solar cells fabricated by blade coating in ambient air ($T = 23\text{ }^{\circ}\text{C}$, $\text{RH} \approx 50\%$) without the benefits of anti-solvent drip or a moisture-free environment. We investigated the solidification process during blade coating of single-cation (FAPbI₃) and increasingly complex mixed-cation mixed-halide (FA_{0.8}MA_{0.15}CS_{0.05}PbI_{2.55}Br_{0.45}, MA is methylammonium) perovskites *in situ* using time-resolved grazing incidence wide-angle X-ray scattering (GIWAXS). We found that the perovskite precursor composition and the blade coating temperature profoundly influence the crystallization mechanism and whether halide segregation occurs. The inclusion of Br⁻ suppresses the non-perovskite 2H phase, promoting instead PbI₂ together with the intermediate 6H phase and 3C phase of FAPbI_{2.55}Br_{0.45}. Addition of Cs⁺ suppresses these intermediates and promotes the direct crystallization of the perovskite 3C phase FA_{0.8}MA_{0.15}CS_{0.05}PbI_{2.55}Br_{0.45} when coating at elevated temperature, unlike when anti-solvent drip is used at room temperature. Through control of ink formulation and coating conditions, we demonstrate blade coated perovskite solar cells with a champion power conversion efficiency (PCE) of 18.20 % as compared with FAPbI₃ perovskites, which yield a PCE of 12.35 % in similar conditions without the benefit of anti-solvent drip. This study provides valuable insight into the crystallization pathway of mixed-cation mixed-halide formulations without anti-solvent drip in high-temperature processing conditions that enable the translation of perovskites toward upscalable ambient manufacturing in high throughput conditions.

Introduction

Hybrid organic-inorganic metal-halide perovskites have impressed the semiconductor community thanks to their remarkable optoelectronic properties, including low exciton binding energy, a sharp absorption onset, and a small Urbach energy despite being prepared via low-cost solution-processing approaches.¹⁻⁴ Hybrid organic-inorganic metal-halide perovskites feature the characteristic AMX₃ structure, where A is an organic or inorganic monovalent

cation, most often methylammonium (MA⁺), formamidinium (FA⁺) or cesium (Cs⁺), M is a metal cation, such as lead (Pb²⁺) or tin (Sn²⁺), and X is a monovalent anion such as chloride (Cl⁻), bromide (Br⁻), iodide (I⁻), and the mixture.^{5,6} Hybrid perovskite thin films are most commonly processed through a one-step spin-coating method, whereby a precursor ink is cast onto a substrate and spun up, an anti-solvent is dripped at the opportune time and the resulting film is subsequently annealed to acquire the desirable perovskite phase. To date, anti-solvent dripping has been the primary approach applied to the one-step spin-coating planar heterojunction small-scale perovskite solar cells with certified power conversion efficiency (PCE) now surpassing 25 %.⁷ Recently, hybrid perovskite compositions have been predominantly based on FA⁺ as the major cation since the α -FAPbI₃ perovskite has a bandgap of 1.48 eV, which is closer to the ideal bandgap of Shockley-Queisser single-junction solar cell (1.34 eV) than classical MAPbI₃ (1.57 eV).⁸ However, the photo-active α -FAPbI₃ perovskite is thermodynamically unstable in ambient air and tends to transform into a non-perovskite yellow δ -FAPbI₃ phase. The incorporation of MA⁺, Cs⁺, and Rb⁺ has been demonstrated to improve the issue of phase instability and results in more stable and efficient multi-component perovskite solar cells.^{9,10} Moreover, mixed-cation (MA⁺, FA⁺, Cs⁺) and mixed-halide (I⁻ and Br⁻) based perovskite solar cells are more reproducible, have a wider

^a King Abdullah University of Science and Technology (KAUST), KAUST Solar Center (KSC), and Physical Science and Engineering Division (PSE), Thuwal, 23955-6900, Saudi Arabia.

^b Key Laboratory of Applied Surface and Colloid Chemistry, National Ministry of Education, Shaanxi Key Laboratory for Advanced Energy Devices, and Shaanxi Engineering Lab for Advanced Energy Technology, School of Materials Science and Engineering, Shaanxi Normal University, Xi'an 710119, China.

^c Department of Materials Science and Engineering, North Carolina State University, Raleigh, NC, 27695, USA.

^d NSLS-II, Brookhaven National Laboratory (BNL), Upton, NY 11973, USA.

^e Cornell High Energy Synchrotron Source (CHESS), Cornell University, Ithaca, NY 14850, USA.

*Electronic Supplementary Information (ESI) available: [details of any supplementary information available should be included here]. See DOI: 10.1039/x0xx00000x

antisolvent processing window, and thermally more stable with higher solar cell performance.^{11, 12}

Despite the current success of high-efficiency small-scale devices via spin coating combined with anti-solvent dripping, scalable printing methods are needed to address upscaling and manufacturability challenges including material and solvent waste, limitation to small-area fabrication, and overall lack of reproducible device-to-device performance.¹³⁻¹⁹ Scalable solution-processing techniques adapted to polycrystalline hybrid perovskite thin films to date include blade coating, slot-die coating, dip coating, spray-coating, and inkjet printing.^{16, 19-25} To date, the blade coating process remains one of the most popular and facile implementations for fabricating high-quality hybrid perovskite thin films and effort has been made to improve the device efficiency and stability.^{13, 15, 26, 27} For instance, Huang's group reported a high PCE of $\approx 19\%$ for MA-rich mixed cations and halides ($\text{MA}_{0.6}\text{FA}_{0.38}\text{Cs}_{0.02}\text{PbI}_{2.975}\text{Br}_{0.025}$) perovskite photovoltaics inside a N_2 glove box.²⁷ The device performance is highly related to the perovskite morphology and crystallization, which, in turn, influence optoelectronic properties such as defect and trap state densities.²⁸⁻³⁰ Despite the apparent simplicity of the blade coating process, the mechanisms underlying the film formation from precursor inks to solid-state thin films, as well as the process-structure relationships are poorly understood. This is partly due to a reliance upon *ex situ* characterization methods, which do not capture the phase transformation behaviour or the formation of intermediate phases. The ability to investigate film formation from the blade coating process via *in situ* techniques is likely to be an essential step toward enabling transition to scalable manufacturing.

For this purpose, *in situ* time-resolved grazing incidence wide-angle X-ray scattering (GIWAXS) has recently emerged as a powerful technique to investigate and track the microstructure evolution of perovskite precursor inks during solution-casting into solid-state perovskite thin films and to investigate the crystallization distribution and orientation in real time. Gong *et al.* examined the classical MAPbI_3 perovskite solution using *in situ* GIWAXS methods and identified the existence of sol-gel disordered nanoparticles, solvated crystalline intermediates, and the polycrystalline perovskite phase during mini-slot-die printing.³¹ Our group revealed, through *in situ* investigations of film formation during spin-coating and blade coating, that significant differences exist in the phase transformation pathway of MAPbI_3 perovskite in these two processes.^{19, 32, 33} We further showed that the processing temperature mediates the structure, halide composition, and polymorph of the solvated intermediate phase, while high-temperature processing ($> 100\text{ }^\circ\text{C}$) circumvented the crystalline solvated phase entirely, thus changing the phase transformation behavior.^{19, 33, 34} The FA-rich mixed cations and mixed halide perovskites ($\text{FA}_{1-x-y}\text{MA}_x\text{Cs}_y\text{PbI}_{3-z}\text{Br}_z$) have recently demonstrated superior device performance, stability and ease of processing as compared to classical MAPbI_3 and FAPbI_3 , but they also benefit from the crucial anti-solvent dripping step which mediates their phase transformation and can kinetically suppress halide segregation.^{9, 35} The incompatibility of the drip with blade coating and meniscus-guided coating techniques in general requires alternative means of control over the phase transformation of the perovskite phase.³⁶ A comprehensive understanding of the phase transition including microstructural and phase evolutions is missing for conditions representative of such scalable manufacturing processes for these complex perovskite compounds. During blade coating, the elevated stage temperature has been found to affect the quality of hybrid perovskite thin films critically in case of MAPbI_3 ,

which otherwise tends to crystallize through solvated intermediate phases that cause pinhole formation.^{19, 32} However, the phase transition is drastically different in FA-rich perovskites, which form non-solvated intermediate hexagonal phases which promote halide segregation in mixed halide perovskites. We, therefore, seek to provide a rational pathway toward the translation of mixed halide mixed cation perovskites toward scalable manufacturing in ambient conditions.

Herein, we compare and contrast four representative perovskite systems (FAPbI_3 , $\text{FAPbI}_{2.55}\text{Br}_{0.45}$, $\text{FA}_{0.8}\text{MA}_{0.15}\text{Cs}_{0.05}\text{PbI}_3$, and $\text{FA}_{0.8}\text{MA}_{0.15}\text{Cs}_{0.05}\text{PbI}_{2.55}\text{Br}_{0.45}$) in terms of their dynamical microstructure evolutions and conversion processes during blade coating by performing *in situ* GIWAXS measurements. With this investigation, we unveil the relationship between the solidification pathway and the effect of the mixed cations and halides at different temperatures without resorting to anti-solvent drip. We adopt the widely used nomenclature for metal oxide perovskites and proposed by Gratia *et al.* to specify the crystal structure of phases associated with the formation of perovskite thin films.³⁷ For example, intermediate phases such as hexagonal 2H, 4H, 6H are often referred to as δ phase; while the cubic 3C perovskite phase is often referred to as α phase. The acronyms 2H, 4H, 6H, and 3C refer to the well-established Ramsdell notation widely used for describing oxide perovskite polytypes.³⁸ In the case of FAPbI_3 , blade coating at $120\text{ }^\circ\text{C}$ reveals the formation of a yellow non-perovskite 2H (100) phase formed within 10 s. By incorporating a small amount of Br⁻ into FAPbI_3 , the 2H (100) phase is suppressed at the expense of the desired perovskite 3C (100) phase, but this forms weakly and is accompanied with PbI_2 formation, pointing to halide segregation. Incorporation of MA^+ and Cs^+ into FAPbI_3 ink (resulting in $\text{FA}_{0.8}\text{MA}_{0.15}\text{Cs}_{0.05}\text{PbI}_3$ composition) promotes formation of the non-perovskite 2H (100) phase and perovskite 3C (100) phase from the disordered sol-gel precursor. By addition of Cs^+ and MA^+ into the system to obtain $\text{FA}_{0.8}\text{MA}_{0.15}\text{Cs}_{0.05}\text{PbI}_{2.55}\text{Br}_{0.45}$ perovskite ink – one of the most popular perovskite compositions yielding efficient solar cells nowadays – the undesired intermediate phases (2H, 6H, and PbI_2) are suppressed when processing at elevated temperature and give way to formation of the desired perovskite 3C phase exclusively without the need for anti-solvent drip. Using these insights, we achieved maximum/average PCEs of 18.2%/16.4% for $\text{FA}_{0.8}\text{MA}_{0.15}\text{Cs}_{0.05}\text{PbI}_{2.55}\text{Br}_{0.45}$ based on planar heterojunction n-i-p devices made with the blade coated hybrid perovskite films in ambient air with 50 R.H.%. In comparison we obtained maximum/average PCEs of 16.3%/14.1% for $\text{FA}_{0.8}\text{MA}_{0.15}\text{Cs}_{0.05}\text{PbI}_3$, 15.8%/13.9% for $\text{FA}_{0.85}\text{MA}_{0.15}\text{PbI}_{2.55}\text{Br}_{0.45}$, 13.9%/11.6% for $\text{FAPbI}_{2.55}\text{Br}_{0.45}$, and 12.4%/9.0% for FAPbI_3 .

Results and discussion

Crystallization Behavior of $\text{FA}_{1-x-y}\text{MA}_x\text{Cs}_y\text{PbI}_{3-z}\text{Br}_z$ Inks via Blade Coating

Blade coating experiments were conducted using a custom-built setup described elsewhere^{35, 39}, and were computer-controlled remotely while performing both *in situ* and *ex situ* GIWAXS measurements at the D1 beamline of the Cornell High Energy Synchrotron Source (CHESS).^{19, 33, 35, 36, 39-46} The integration time for individual GIWAXS snapshots was 0.2 s, allowing a frame rate of 5 Hz, sufficient to capture the phase transformation behaviour in blade coating experiments performed in this study.

ARTICLE

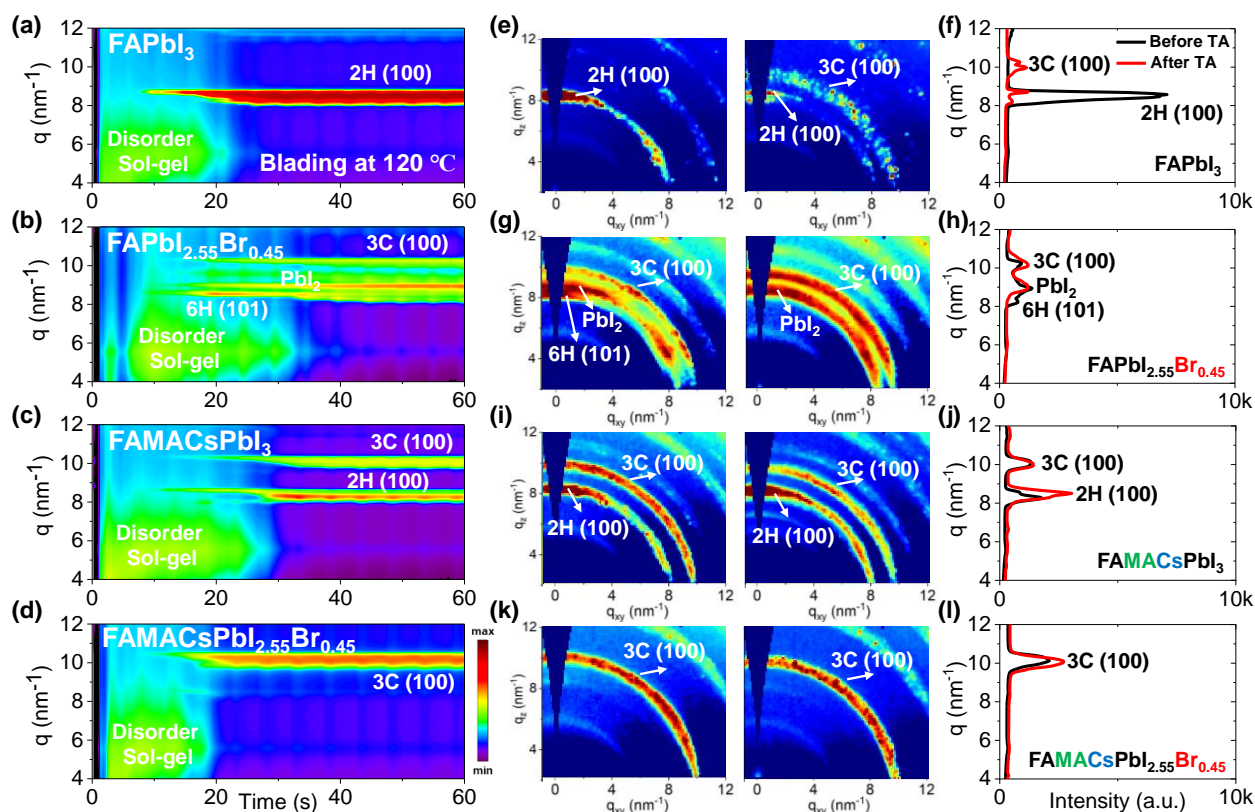


Fig. 1 *In situ* 2D GIWAXS scattering evolution vs. time for various perovskite precursor formulations showing ink-to-solid transformation during blade coating for (a) FAPbI₃, (b) FAPbI_{2.55}Br_{0.45}, (c) FA_{0.8}MA_{0.15}CS_{0.05}PbI₃, and (d) FA_{0.8}MA_{0.15}CS_{0.05}PbI_{2.55}Br_{0.45}. Representative 2D GIWAXS snapshots taken at the final stage of blade coating as well as post-annealing (10 minutes at 100 °C), together with a plot of q vs. intensity are shown for (e, f) FAPbI₃, (g, h) FAPbI_{2.55}Br_{0.45}, (i, j) FA_{0.8}MA_{0.15}CS_{0.05}PbI₃, and (k, l) FA_{0.8}MA_{0.15}CS_{0.05}PbI_{2.55}Br_{0.45}. Scattering features associated with the disordered sol-gel phase and yellow non-perovskite 2H (100) phase ($q = 8.5 \text{ nm}^{-1}$) are identified along with the (100) diffraction of Pbl₂ ($q = 9.0 \text{ nm}^{-1}$) and perovskite 3C (110) phase diffraction ($q = 10.2 \text{ nm}^{-1}$).

We began our investigations by comparing the blade coating of FA-dominated triiodide and mixed halide systems, including FAPbI₃ and FA_{0.8}MA_{0.15}CS_{0.05}PbI₃, as well as FAPbI_{2.55}Br_{0.45} and FA_{0.8}MA_{0.15}CS_{0.05}PbI_{2.55}Br_{0.45}. All formulations were prepared with the same molarity (1.2 M) in a mixture of N,N-dimethylformamide (DMF) and dimethyl sulfoxide (DMSO) solvents with a 4:1 volume ratio. In **Fig. 1a-d**, we present the time-evolutions of 2D X-ray scattering intensity with respect to the scattering vector (q) for the perovskite ink formulations mentioned above. Representative 2D GIWAXS snapshots collected at 5, 20, and 60 s during blade coating at 120 °C of all perovskite ink formulations are also shown in **Fig. S1**. The length of the scattering vector q is determined by the following equation: $q = \sqrt{q_z^2 + q_{xy}^2}$, where: $q_z = \frac{4\pi \sin \alpha_f}{\lambda}$, $q_{xy} = \frac{4\pi \sin \theta_f}{\lambda}$, λ is the wavelength.^{43,47,48} The emergent waves with the momentum can be described by the in-plane exit angle α_f and the out-of-plane angle θ_f (with respect to the scattering plane).⁴⁹ Blade coating experiments were performed on compact TiO₂-coated glass substrates for 60 s at a coating speed of 25 mm/s. The sample holder was pre-heated to

120 °C and as-cast films were subjected to an additional annealing step at 100 °C for 10 minutes, after which an additional *ex situ* GIWAXS measurement was performed.

The time-evolution of the scattering features of FAPbI₃ (**Fig. 1a**) reveal a solvated, colloidal sol precursor during the first 20 s, as indicated by the formation of a scattering halo at low q values (4 to 8 nm⁻¹).⁵⁰ The hexagonal (non-perovskite) 2H (100) phase^{9,12,37,38} ($q \approx 8.5 \text{ nm}^{-1}$) forms around 10 s, coexisting with the colloidal sol state for ~10 s. The 2H (100) phase scattering intensifies significantly with the disappearance of the sol scattering signal for $t > 20$ s and is subsequently the only scattering feature observed in the as-cast film, indicating the ink has solidified and converted to the 2H (100) phase. The 2H phase formed in the as-cast film tends to be highly textured with the c-axis normal to the substrate plane (**Fig. 1e**). Upon annealing, the FAPbI₃ film converts partially to the perovskite 3C (100) phase and exhibits weak diffraction intensity (**Fig. 1f**). This is not surprising as the annealing temperature required for full conversion has been reported to be above 150 °C.^{51,52}

Addition of a small amount of Br⁻ into the formulation (nominally FAPbI_{2.55}Br_{0.45}) complicates the crystallization outcome considerably

(Fig. 1b). The as-cast film yields three phases: the 6H (101) phase^{9, 12, 37, 38} forms most prominently at first, along with PbI_2 ($q = 9.0 \text{ nm}^{-1}$) and the perovskite 3C (100) phase^{9, 12, 37, 38} ($q = 10.2 \text{ nm}^{-1}$). However, the 6H (101) phase seems unstable as its intensity weakens significantly after $\sim 30 \text{ s}$ (Fig. 1g). Upon thermal annealing, the 6H (101) phase disappears completely, leaving behind a partially converted film composed of a mixture of crystalline PbI_2 and 3C (100) perovskite phases (Fig. 1h). Addition, instead, of small fractions of MA^+ and Cs^+ into the triiodide formulation (nominally $\text{FA}_{0.8}\text{MA}_{0.15}\text{Cs}_{0.05}\text{PbI}_3$) (Fig. 1c) suppresses PbI_2 formation and promotes the formation of the perovskite 3C (100) phase in addition to the 2H (100) phase (Fig. 1i). Thermal annealing does not appreciably alter the as-cast film's state and appears to promote 2H (100) phase formation (Fig. 1j).

In Fig. 1d, we reveal that simultaneously incorporating small amounts of MA^+ and Cs^+ into the previous $\text{FAPbI}_{2.55}\text{Br}_{0.45}$ ink (resulting in the $\text{FA}_{0.8}\text{MA}_{0.15}\text{Cs}_{0.05}\text{PbI}_{2.55}\text{Br}_{0.45}$ nominal composition) tends to form the desired perovskite 3C (100) phase directly from the disordered sol precursor without forming intermediate non-perovskite phases, such as 2H, 6H phases and PbI_2 . It is important to recognize that the phase transformation of the solution by blade coating at elevated temperature is very different from that of spin coating and appears to emulate the effects of anti-solvent drip without the kinetic quenching.^{9, 53} In contrast to the previous three Cs-free perovskite formulations, the Cs-containing formulation ($\text{FA}_{0.81}\text{MA}_{0.14}\text{Cs}_{0.05}\text{PbI}_{2.55}\text{Br}_{0.45}$) starts to show perovskite phase (3C (100) phase, $q = 10.2 \text{ nm}^{-1}$) at around 20s during blade coating. The as-cast $\text{FA}_{0.81}\text{MA}_{0.14}\text{Cs}_{0.05}\text{PbI}_{2.55}\text{Br}_{0.45}$ thin film exhibits a strong feature of the 3C (100) perovskite phase, which further increases its diffraction intensity after thermal annealing (Fig. 1k and l). Importantly, the non-perovskite 2H phase has a negligible signal, indicating that the 3C phase dominates the microstructure. Thus, we found that the main factors that could have an enormous impact on the microstructural evolution relate very much to the original composition of the perovskite ink before heat treatment, and that presence of Cs^+ and Br^- promotes the formation of the perovskite 3C phase exclusively without other intermediate phases.

Nominal formula	FAPbI_3	$\text{FAPbI}_{2.55}\text{Br}_{0.45}$	FAMACsPbI_3	$\text{FAMACsPbI}_{2.55}\text{Br}_{0.45}$
Phases present	2H	6H, PbI_2 , 3C	2H, 3C	3C
Perovskite phase formed?	No	Yes	Yes	Yes
Non-perovskite phase(s) present?	Yes	Yes	Yes	No

Table 1 Summary of the phases formed during blade coating at 120 °C of different FA-based formulations, including FAPbI_3 , $\text{FAPbI}_{2.55}\text{Br}_{0.45}$, $\text{FA}_{0.8}\text{MA}_{0.15}\text{Cs}_{0.05}\text{PbI}_3$, and $\text{FA}_{0.8}\text{MA}_{0.15}\text{Cs}_{0.05}\text{PbI}_{2.55}\text{Br}_{0.45}$ in a solvent mixture of DMF and DMSO.

We summarize the *in situ* GIWAXS findings in Table 1. FAPbI_3 formulation forms the non-perovskite yellow 2H (100) phase from a disordered sol precursor. Addition of a small amount of Br^- ($\text{FAPbI}_{2.55}\text{Br}_{0.45}$) suppress the 2H phase and generates the desired 3C perovskite phase together with undesirable PbI_2

crystals, indicative of halide segregation in the as-cast film. Further addition of Cs^+ ($\text{FA}_{0.8}\text{MA}_{0.15}\text{Cs}_{0.05}\text{PbI}_{2.55}\text{Br}_{0.45}$) further suppresses the intermediate non-perovskite 2H phase and promotes single perovskite 3C phase formation.

Impact of Coating Temperature on Phase Formation

The processing temperature was previously reported to play an essential role in the phase transformation behaviour of perovskite films.^{19, 32-34} Blade coating at elevated temperature has yielded higher quality films and better photovoltaic performance than films prepared at a lower temperature. To understand the impact of the blading temperature on the phase conversion of mixed-halide mixed-cation systems, we have compared the phase transformation behaviours of $\text{FA}_{0.8}\text{MA}_{0.15}\text{Cs}_{0.05}\text{PbI}_{2.55}\text{Br}_{0.45}$ formulations blade coated at low (60 °C) and high (120 °C) temperatures. Fig. 2a and b show 2D maps (with integration of each time slice) of the scattering intensity q (ordinate; $4 < q < 12 \text{ nm}^{-1}$) tracked over time (abscissa; $0 < t < 360 \text{ s}$ for blading at 60 °C and $0 < t < 60 \text{ s}$ for blade coating at 120 °C, respectively). Representative 2D GIWAXS snapshots collected during blade coating at 60 and 120 °C are summarized in Fig. S2. Fig. 2a shows the time evolution of phase transformation at 60 °C. Prior to $\approx 210 \text{ s}$, we observe the wet sol colloidal precursor, as indicated by the scattering halo at low q values (4 to 7 nm^{-1}).^{19, 32} Subsequently, two diffraction features appear close to the 3C perovskite: a Br-poor 3C perovskite α_1 phase at $q = 9.9 \text{ nm}^{-1}$ and a Br-rich 3C perovskite α_2 phase (at $q = 10.3 \text{ nm}^{-1}$). These are accompanied by the formation of PbI_2 crystals ($q = 9.0 \text{ nm}^{-1}$) and the non-perovskite 4H phase (100)^{9, 12, 37, 38} ($q \approx 8.36 \text{ nm}^{-1}$). These results prove the phase transformation behaviour promotes halide segregation in the perovskite phase, resulting simultaneously in Br-poor and Br-rich 3C structures as PbI_2 crystals and the non-perovskite 4H phase form, respectively. This leads to perovskite 3C phases exhibiting different energetics and bandgaps, expected to act as recombination sites with a negative impact on the performance of solar cells. On the other hand, blade coating at 120 °C (Fig. 2b) forms the desired perovskite 3C (100) phase directly and exclusively, providing no apparent cause for halide segregation. The 3C phase forms directly from the disordered sol at around 20 s. The fact that non-perovskite phases are not observed suggests that thermal energy favours the nucleation and growth of the entropically stabilized mixed halide mixed cation 3C phase and that rapid drying of the solution due to hot casting does not quench the system into alternative phases.^{9, 53} A schematic representation of the solidification pathway of $\text{FA}_{0.8}\text{MA}_{0.15}\text{Cs}_{0.05}\text{PbI}_{2.55}\text{Br}_{0.45}$ perovskite thin films at low and elevated temperatures is shown in Fig. 2c. At low temperature, slow drying leads to the formation of halide-segregated perovskite 3C phases (Br-poor and Br-rich), along with non-perovskite PbI_2 crystals and the 4H (100) phase. The film achieves poor surface coverage as per scanning electron microscopy (SEM) images (Fig. S3). At high temperature, the perovskite crystals nucleate and grow directly

from the colloidal sol, forming compact films as confirmed in the SEM micrographs shown in Fig. 3a. Representative 2D GIWAXS snapshots at the final stage of blade coating (at 360 s for 60 °C and at 60 s for 120 °C) for the $\text{FA}_{0.8}\text{MA}_{0.15}\text{Cs}_{0.05}\text{PbI}_{2.55}\text{Br}_{0.45}$ perovskite thin films are plotted in Fig. 2d. We further plot in Fig. 2e the intensity versus q (at 60 s) and the time-evolution of intensity at $q = 10.2 \text{ nm}^{-1}$, confirming the perovskite 3C phase forms a single intense phase and does so very rapidly at 120 °C, whereas low-temperature processing leads to the formation of competing phases with distinct halide composition which cause halide-segregation when converted to the perovskite phase.

Previous UV-Vis absorbance studies of lead iodide and lead-bromide solutions in DMF and DMSO have revealed significant differences in the formation of lead-solvent complexes known as iodoplumbates and bromoplumbates. Lead bromide tends to

complex more weakly with solvents and forms metal-rich clusters whereas lead iodide complexes strongly with DMSO.⁵⁴⁻⁵⁶ It is reasonable to assume that a slow drying sol precursor containing a mixture of lead iodide and lead bromide in the presence of DMSO and DMF should promote halide segregation by preferential loss of solvent from the bromoplumbate sol while iodoplumbate sol remains highly solvated, thus promoting the formation of Br-rich and I-rich regions of the as-cast sol and leading to formation of PbI_2 and other phases. Hot casting enhances the drying kinetics while also providing thermal energy in favor of the phase transformation of the thermodynamically favored mixed halide, mixed cation perovskite phase.

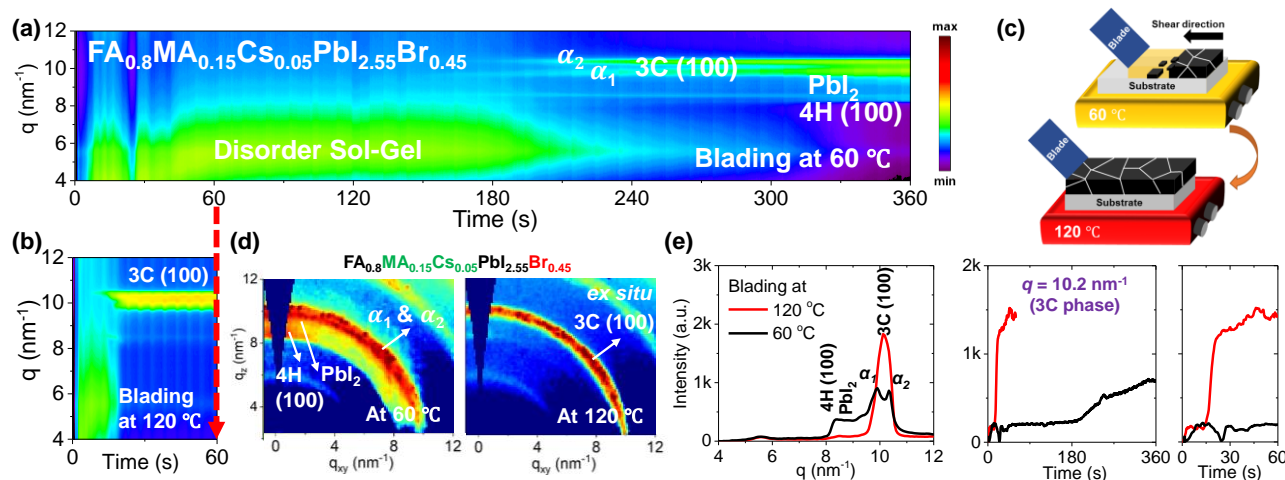


Fig. 2 *In situ* 2D GIWAXS intensity map of the $\text{FA}_{0.8}\text{MA}_{0.15}\text{Cs}_{0.05}\text{PbI}_{2.55}\text{Br}_{0.45}$ perovskite precursor inks showing ink-to-solid transformation during blade coating (a) at 60 °C and (b) 120 °C. (c) Schematic representation of the $\text{FA}_{0.8}\text{MA}_{0.15}\text{Cs}_{0.05}\text{PbI}_{2.55}\text{Br}_{0.45}$ perovskite thin film formation mechanism at low 60 °C and high 120 °C blade coating temperatures. (d) Representative 2D GIWAXS snapshots taken at the final stage of blade coating perovskite films for $\text{FA}_{0.8}\text{MA}_{0.15}\text{Cs}_{0.05}\text{PbI}_{2.55}\text{Br}_{0.45}$ at 60 °C and 120 °C, respectively. (e) Scattering vector q versus intensity distribution of $\text{FA}_{0.8}\text{MA}_{0.15}\text{Cs}_{0.05}\text{PbI}_{2.55}\text{Br}_{0.45}$ perovskite film at final stage of blade coating and time evolution of the diffraction intensity related to perovskite 3C (100) phase ($q = 10.2 \text{ nm}^{-1}$) for $\text{FA}_{0.8}\text{MA}_{0.15}\text{Cs}_{0.05}\text{PbI}_{2.55}\text{Br}_{0.45}$ perovskite ink at 60 °C and 120 °C.

Morphology and Optoelectronic Properties

We have investigated the resultant thin film morphology of all five formulations after coating and thermal annealing with the help of SEM. At low magnification, the films appear to form continuous and compact films with large domains across the substrate (Fig. 3a). However, inspection at higher magnification reveals several pinholes in FAPbI_3 and $\text{FAPbI}_{2.55}\text{Br}_{0.45}$ films and extended cracks between domains in $\text{FA}_{0.85}\text{MA}_{0.15}\text{PbI}_{2.55}\text{Br}_{0.45}$ and $\text{FA}_{0.8}\text{MA}_{0.15}\text{Cs}_{0.05}\text{PbI}_3$ films. Under these blade coating conditions, it appears that only $\text{FA}_{0.8}\text{MA}_{0.15}\text{Cs}_{0.05}\text{PbI}_{2.55}\text{Br}_{0.45}$ films exhibit high structural quality, free of pinholes or cracks. The origin of these pinholes and cracks is not entirely understood but is not entirely surprising given the volume change that intermediate phases must undergo to transform into the 3C phase. Furthermore, the thermal expansion coefficient of hybrid perovskites tends to be an order of magnitude higher than that of typical inorganic substrates⁵⁷,

causing cracking-induced stress relaxation during cooling, not unlike other semiconductors exhibiting large mismatch of thermal expansion coefficient.⁵⁸

We investigate the structure and properties of the above films (Fig. 3b, 3c, and S6), as well as additional films prepared at an elevated coating temperature (150 °C, to overcome the challenges of processing translation from low to high humidity ambient conditions). This was found to promote the formation of higher quality films than at 120 °C, which we attribute tentatively and partly to humid ambient conditions in our lab ($T = 23 \text{ °C}$, $\text{RH} \approx 50\%$), as well as to the higher processing temperature which promote formation of the thermodynamically favored phase and at the same time rapidly dry the solution, thus kinetically inhibiting precursor segregation. Optical photographs of all five representative blade coated perovskite thin films at 120 and 150 °C are summarized in Fig. S4a. The spectral absorbance of FAPbI_3 and

FAPbI_{2.55}Br_{0.45} films do not exhibit a clear absorption onset compared to the other perovskite systems. We attribute this to incomplete perovskite phase conversion after blade coating at 150 °C and possible decomposition in humid ambient air, as evidenced by the appearance of 2H, 6H and PbI₂ phases in *ex situ* XRD analysis (Fig. 3c and S6). By contrast, the FA_{0.8}MA_{0.15}CS_{0.05}PbI₃ solid-state thin film exhibits a characteristic perovskite absorbance onset at around 800 nm, while the addition of a small quantity of Br⁻ for the FA_{0.85}MA_{0.15}PbI_{2.55}Br_{0.45} and FA_{0.8}MA_{0.15}CS_{0.05}PbI_{2.55}Br_{0.45} films resulted in a blue shift of the bandgap onset (absorbance onset is around 770 nm). The variation of cations was found to have little impact on the bandgap of the studied perovskites, but the addition of Cs⁺ into the perovskite structure increases the absorbance of FA_{0.8}MA_{0.15}CS_{0.05}PbI_{2.55}Br_{0.45} perovskite thin films for $\lambda < 750$ nm, owing to its propensity to form the 3C phase. The FA_{0.8}MA_{0.15}CS_{0.05}PbI_{2.55}Br_{0.45} film shows the most intense 3C phase reflection (14.0°) among all perovskite cases studied, whereas FAPbI₃ and FAPbI_{2.55}Br_{0.45} films show evidence of non-perovskite intermediate 2H and PbI₂ phases when blade coating at 120 °C. However, FA_{0.85}MA_{0.15}PbI_{2.55}Br_{0.45}, FA_{0.8}MA_{0.15}CS_{0.05}PbI_{2.55}Br_{0.45}, and FA_{0.8}MA_{0.15}CS_{0.05}PbI₃ perovskite solutions formed the desired perovskite 3C phase exclusively when blade coated at 150 °C, improving upon the outcome of deposition at 120 °C.

We have investigated how the composition of the perovskite film influences its trap state density and charge mobility using space charge limited current (SCLC)

measurements. We collected the dark current–voltage characteristics for electron-only devices with glass/fluorine-doped tin oxide (FTO)/compact titanium dioxide (c-TiO₂)/blade coated perovskite/[6,6]-phenyl-C₆₁-butyric acid methyl ester (PCBM)/silver (Ag) architecture for various perovskite thin films (see Fig. S5 for the other perovskites).⁵⁰ Fig. 3d illustrates the dark current–voltage characteristics of the representative mixed-cation mixed-halide perovskite FA_{0.8}MA_{0.15}CS_{0.05}PbI_{2.55}Br_{0.45}, indicating a linear ohmic response at a low bias (< 0.11 V), a trap-filling regime (0.12 to 0.61 V) and a trap-free SCLC regime (> 0.62 V). The trap state density was determined by the trap-filled limit voltage using the following equation: $N_t = \frac{2\epsilon_0\epsilon_r V_{TFL}}{qL^2}$, where ϵ_0 is the vacuum permittivity, ϵ_r is the relative dielectric constant, V_{TFL} is the onset voltage of the trap-filled limit region, q is the elemental charge, and L is the thickness of the film.⁵⁹ We found that the trap-state densities are similar for FAPbI₃ and FAPbI_{2.55}Br_{0.45} perovskite films, which are on the order of 2×10^{16} cm⁻³. Trap densities decrease slightly to 1.8×10^{16} , 1.9×10^{16} and 0.9×10^{16} cm⁻³ for FA_{0.85}MA_{0.15}PbI_{2.55}Br_{0.45}, FA_{0.8}MA_{0.15}CS_{0.05}PbI₃, and FA_{0.8}MA_{0.15}CS_{0.05}PbI_{2.55}Br_{0.45}, respectively (Fig. 3e). These results indicate that the introduction of Cs⁺ and Br⁻ simultaneously remediates defects in the perovskite thin film. This is consistent with *in situ* observations that a single perovskite 3C phase forms during blade coating, resulting in ion uniformity throughout the film, with the benefit of reduced charge recombination and possibly increased FF in solar cell devices.

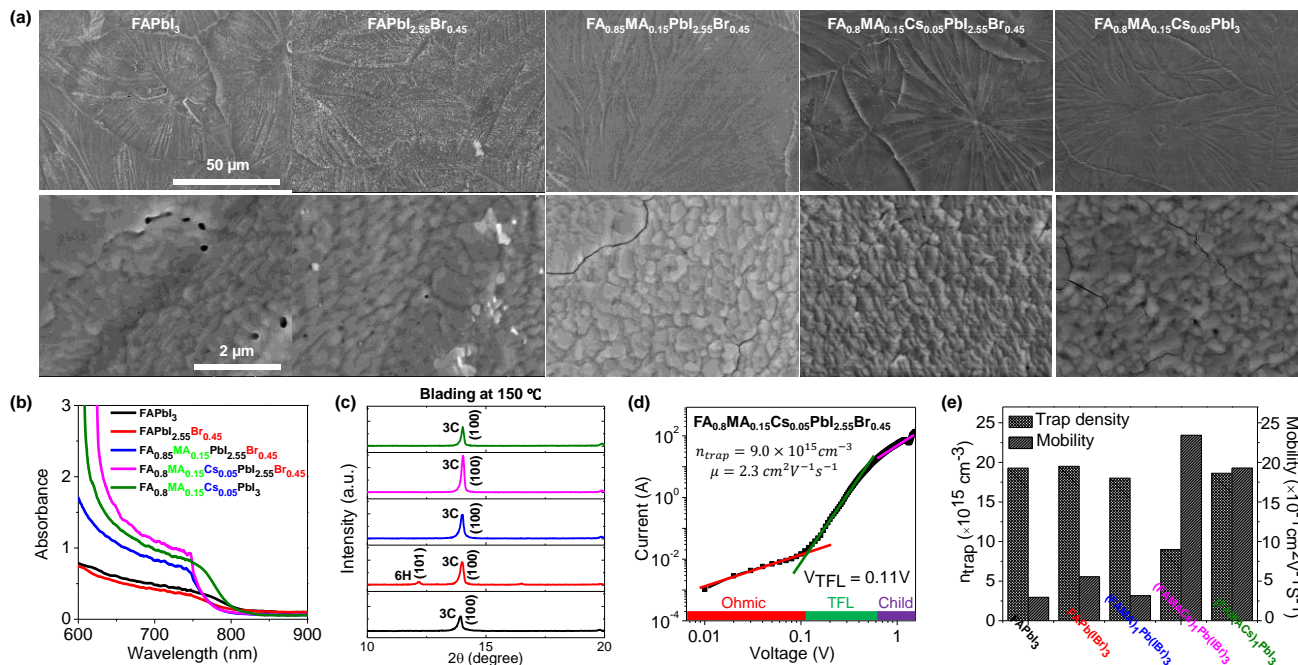


Fig. 3 Comparison of FAPbI₃, FAPbI_{2.55}Br_{0.45}, FA_{0.85}MA_{0.15}PbI_{2.55}Br_{0.45}, FA_{0.8}MA_{0.15}CS_{0.05}PbI_{2.55}Br_{0.45} and FA_{0.8}MA_{0.15}CS_{0.05}PbI₃ films via blade coating. (a) Top-view SEM images of perovskite films prepared using the blade coating method at 150 °C (top row shows low magnification while the bottom row shows higher magnification). (b, c) Absorption spectra and XRD patterns of blade coated hybrid perovskite as-cast thin films with different precursor inks. (d) Dark *I*-*V* measurement of the electron-only device displaying V_{TFL} kink point behavior for the representative FA_{0.8}MA_{0.15}CS_{0.05}PbI_{2.55}Br_{0.45} perovskite thin film. (e) Trap density and electron mobility.

ARTICLE

The intrinsic electron mobility was estimated using the SCLC method (Fig. 3e).⁶⁰ The electron mobility is found to be $0.3 \text{ cm}^2 \text{V}^{-1} \text{s}^{-1}$ for the FAPbI₃ film. Introduction of Br⁻, MA⁺, and Cs⁺ together enhance the electron mobility significantly. The electron mobility increases to $0.6 \text{ cm}^2 \text{V}^{-1} \text{s}^{-1}$ with the addition of Br⁻ and further increases for FA_{0.8}MA_{0.15}CS_{0.05}PbI₃ and FA_{0.8}MA_{0.15}CS_{0.05}PbI_{2.55}Br_{0.45} films, to 1.9 and $2.3 \text{ cm}^2 \text{V}^{-1} \text{s}^{-1}$, respectively. These results further show that the microstructural benefits of Cs⁺ and Br⁻ addition also impact the carrier mobility of the film. Meanwhile, the FA_{0.8}MA_{0.15}CS_{0.05}PbI_{2.55}Br_{0.45} ink eliminates all intermediate non-perovskite phases and promotes the perovskite 3C phase formation at elevated temperature, emulating the effects of anti-solvent drip at room temperature.^{9, 53} SCLC measurements confirm that simultaneous introduction of Cs⁺ and Br⁻ in the perovskite structure remedies trap states and enhances the carrier mobility in the perovskite thin film.

Photovoltaic Device Performance and Stability

We fabricated planar n-i-p type perovskite solar cells in ambient air ($T = 23 \text{ }^\circ\text{C}$, RH $\approx 50 \%$) using blade coated perovskite layers in the following configuration (Fig. 4c): glass/ FTO/ c-TiO₂/ blade coated perovskite/ 2,2',7,7'-tetrakis-(*N,N*-dimethoxyphenylamine) 9,9'-spirobifluorene (Sprio-OMeTAD)/ gold (Au)/ Ag. All solar cells were tested under the standard AM 1.5G (air mass 1.5 global 1 Sun) illumination in ambient air ($T = 23 \text{ }^\circ\text{C}$, RH $\approx 50 \%$) with a scan rate of 0.1 Vs^{-1} , and the photovoltaic figures of merit are collected from 30–40 devices for each condition (Fig. 4a), with the statistical distribution of PCE shown in Fig. 4d and summarized in Table S1. The FAPbI₃ device exhibits a PCE of $9.03 \pm 2.44 \%$, with short-circuit current (J_{SC}) of $20.86 \pm 0.82 \text{ mA cm}^{-2}$, fill factor (FF) of $60.63 \pm 1.87 \%$, and open-circuit voltage (V_{OC}) of $0.97 \pm 0.01 \text{ V}$. We observed statistically meaningful PCE improvements with a small amount of Br⁻ halide addition for the FAPbI_{2.55}Br_{0.45} devices to $11.64 \pm 0.89 \%$. Addition of a small amount of MA⁺ for the FA_{0.85}MA_{0.15}PbI_{2.55}Br_{0.45} devices further improves the PCE to $13.89 \pm 0.84 \%$. Incorporation of Cs⁺ to yield the FA_{0.8}MA_{0.15}CS_{0.05}PbI_{2.55}Br_{0.45} film leads to an enhancement of PCE to $16.40 \pm 1.22 \%$, which is the highest value among the five perovskite devices. Interestingly, without Br⁻ (i.e., FA_{0.8}MA_{0.15}CS_{0.05}PbI₃), PCE decreases to $14.10 \pm 0.83 \%$, which is a solid proof of the critical importance of Cs⁺ and Br⁻. This may be attributed to the introduction of Br⁻ which remedies defects in the FA_{0.8}MA_{0.15}CS_{0.05}PbI_{2.55}Br_{0.45} perovskite layer, resulting in higher electron mobility and lower trap density (Fig. 3e). Moreover, this is consistent with time-resolved

investigations that a single perovskite 3C phase forms in FA_{0.8}MA_{0.15}CS_{0.05}PbI_{2.55}Br_{0.45} case (Fig. 1), with the benefit of higher performance in solar cells. Representative reverse and forward J - V scans of FAPbI₃ and FA_{0.8}MA_{0.15}CS_{0.05}PbI_{2.55}Br_{0.45} solar cells are shown in Fig. S7. Due to the synergistic addition of Cs⁺ and Br⁻, it is clear that not only the PCE of devices increase but the hysteresis of J - V curves massively reduces in FA_{0.8}MA_{0.15}CS_{0.05}PbI_{2.55}Br_{0.45} solar cells. The poor performance for the FAPbI₃ device results from bad film quality as shown in Fig. 3a. The significant improvement in efficiency is mainly attributed to the enhancement in FF and J_{SC} , partially due to improved film quality and optoelectronic properties (Fig. 3). These results highlight the need to have the coexistence of small amounts of Cs⁺ and Br⁻. We achieved a champion cell with PCE of 18.20 %, $V_{\text{OC}} = 1.09 \text{ V}$, $J_{\text{SC}} = 22.50 \text{ mA cm}^{-2}$ and $FF = 74.23 \%$ for the FA_{0.8}MA_{0.15}CS_{0.05}PbI_{2.55}Br_{0.45} perovskite solar cell (Fig. 4b), which is one of the highest values reported to date for the FA-rich perovskite devices fabricated at high-speed under realistic conditions. The other representative J - V curves of the remaining perovskite devices under AM1.5G illumination are shown in Figure S4b. We further demonstrated promising light-soaking stability of the cell, with a stabilized PCE of $\approx 17.70 \%$ under 8-minute continuous illumination (Fig. 4c). This stable illumination stability is due to suppressed phase conversion from the perovskite 3C phase to non-perovskite phases mainly assisted by the addition of Cs⁺ and Br⁻ ions.⁶¹

The environmental stability of the corresponding perovskite solar cells was further evaluated. Solar cell devices without encapsulation were exposed to an ambient environment with $\approx 50 \%$ relative humidity in the dark at room temperature. The normalized PCEs versus time were recorded periodically and are reported in Fig. 4e. The FA_{0.8}MA_{0.15}CS_{0.05}PbI₃ and FA_{0.8}MA_{0.15}CS_{0.05}PbI_{2.55}Br_{0.45} devices exhibit significantly improved environmental stability in contrast to the other ones. For example, the PCEs retain 36 %, 35 %, 38 %, 66 % and 63 % of its initial value for the FAPbI₃, FAPbI_{2.55}Br_{0.45}, FA_{0.85}MA_{0.15}PbI_{2.55}Br_{0.45}, FA_{0.8}MA_{0.15}CS_{0.05}PbI₃ and FA_{0.8}MA_{0.15}CS_{0.05}PbI_{2.55}Br_{0.45} solar cells after 36-day ambient exposure in 50 % RH conditions without encapsulation. The far superior ambient stability of FA_{0.8}MA_{0.15}CS_{0.05}PbI₃ and FA_{0.8}MA_{0.15}CS_{0.05}PbI_{2.55}Br_{0.45} devices is partially attributed to fewer phase impurities present in the as-prepared films⁶¹ and to better phase stability since the addition of Cs⁺ and Br⁻ together with high-temperature processing helps to form an entropically stabilized phase.^{9, 53}

ARTICLE

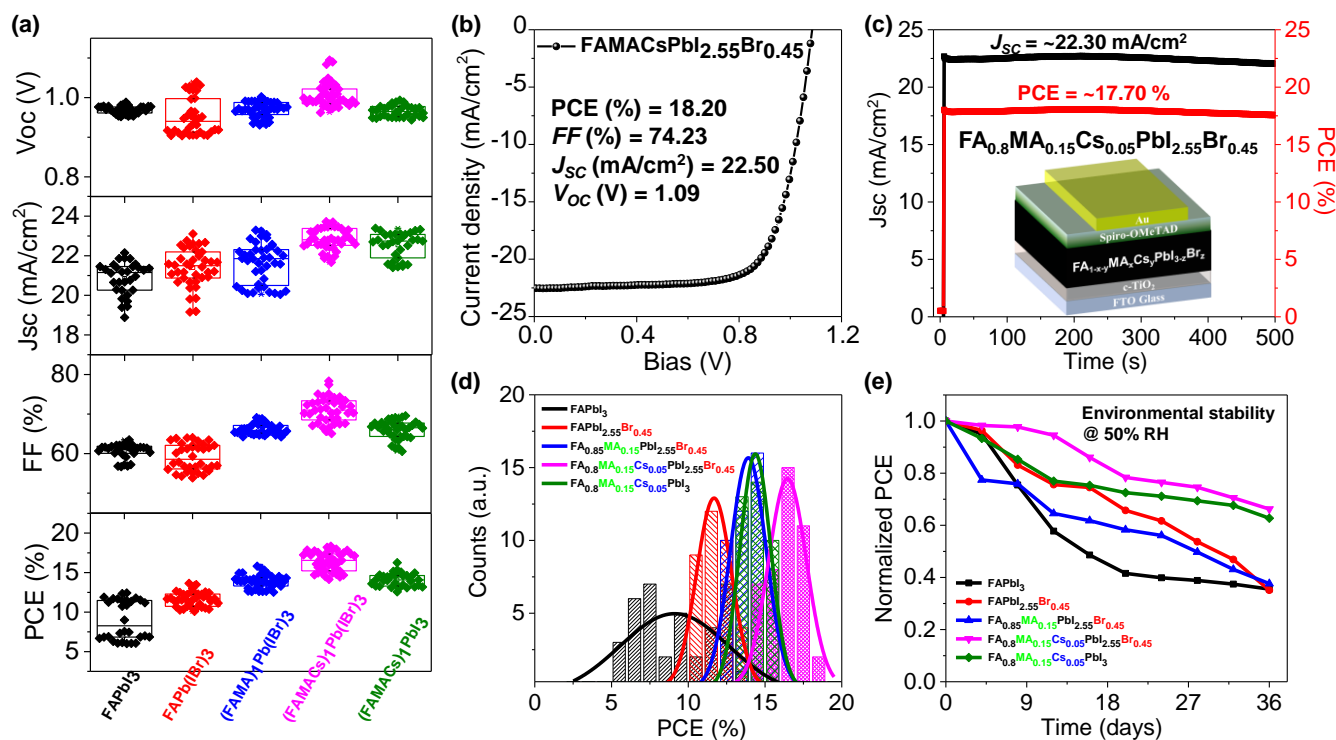


Fig. 4 Solar cell architecture and characterization. (a) Statistics of 30–40 devices for each $\text{FA}_{1-x-y}\text{MA}_x\text{Cs}_\gamma\text{PbI}_{3-z}\text{Br}_z$ perovskite solar cell. (b) J - V curve for the peak efficiency of 18.20% obtained in the $\text{FA}_{0.8}\text{MA}_{0.15}\text{Cs}_{0.05}\text{PbI}_{2.55}\text{Br}_{0.45}$ perovskite solar cell under AM1.5G illumination. (c) The stabilized power output of J_{sc} and PCE is monitored over time at the maximum power point with solar cell architecture. (d) Comparison of photovoltaic PCE distribution employing blade coated perovskite solar cells prepared at 150 °C (approximately 30–40 devices for each composition were measured). (e) Recorded long-term environmental stability of the corresponding FAPbI₃, FAPbI_{2.55}Br_{0.45}, $\text{FA}_{0.85}\text{MA}_{0.15}\text{PbI}_{2.55}\text{Br}_{0.45}$, $\text{FA}_{0.8}\text{MA}_{0.15}\text{Cs}_{0.05}\text{PbI}_{2.55}\text{Br}_{0.45}$, and $\text{FA}_{0.8}\text{MA}_{0.15}\text{Cs}_{0.05}\text{PbI}_3$ perovskite solar cells exposed in an ambient environment with 50% relative humidity without encapsulation.

Conclusions

In summary, we systemically investigated blade coating of FA-based mixed-halide mixed-cation perovskite films to assess how they form without anti-solvent dripping but in the presence of elevated processing temperatures. We focused our attention on the roles played by Cs⁺ and Br⁻ additions on the crystallization pathway in blade coating, associated halide segregation, microstructure, morphology, carrier mobility, trap state formation and solar cell performance. *In situ* time-resolved GIWAXS measurements performed during blade coating of FA-based perovskite formulations at different temperatures reveal a microstructural evolution that is extremely sensitive to the cation and halide formulation as well as to the coating temperature. FAPbI₃ forms the non-perovskite 2H phase from the disordered colloidal sol. Addition of a small amount of Br⁻ to form FAPbI_{2.55}Br_{0.45} strongly suppresses the 6H phase and

generates the desired perovskite 3C phase, but concurrently with the PbI₂ phase. Meanwhile, further addition of Cs⁺ to form $\text{FA}_{0.8}\text{MA}_{0.15}\text{Cs}_{0.05}\text{PbI}_{2.55}\text{Br}_{0.45}$ at elevated temperature eliminates all intermediate non-perovskite phases and promotes the perovskite phase formation. SCLC measurements confirm that simultaneous introduction of Cs⁺ and Br⁻ in the perovskite structure remedies trap states and enhances the carrier mobility in the perovskite thin film. We go on to show that the blade coated solar cell performance is closely linked to the initial formulation of perovskite inks and the performance results obtained are supported by *in situ* GIWAXS observation of the microstructure evolution and whether a single perovskite or multiple non-perovskite phases form. $\text{FA}_{0.8}\text{MA}_{0.15}\text{Cs}_{0.05}\text{PbI}_{2.55}\text{Br}_{0.45}$ solar cells blade coated in ambient air yielded a peak efficiency of 18.20%. To the best of our knowledge, our study is the first one to use *in situ* GIWAXS to shed light on the role of cation (FA⁺, MA⁺, and Cs⁺) and halide (I⁻

, Br) mixing as well as the role of coating temperature on the crystallization pathway of mixed-halide mixed-cation perovskites during blade coating. This insight provides an in-depth understanding of perovskite ink drying and phase transformation without anti-solvent drip, which is critical and very meaningful for perovskite ink design in the future to achieve improved reproducibility in low-cost and large-scale manufacturing of hybrid perovskite photovoltaics.

Conflicts of interest

There are no conflicts to declare.

Acknowledgments

This work was supported by the King Abdullah University of Science and Technology (KAUST), the North Carolina State University (NCSSU) and the National Key Research and Development Program of China (2017YFA0204800, 2016YFA0202403), National Natural Science Foundation of China (61604092, 61674098), National University Research Fund (Grant Nos. GK261001009, GK201603055), the 111 Project (B14041), the National 1000 Talents Plan program (1110010341). GIWAXS measurements were performed at the D-line at the Cornell High Energy Synchrotron Source (CHESS) at Cornell University. CHESS is supported by the NSF via NSF Award DMR-1332208. M.-C. Tang[†] and Y. Fan[†] contributed equally to this work.

Author Contributions

M.-C.T. and A.A. designed and performed most of the time-resolved investigations. Y.F. and X.C. conducted device fabrication and measurements for optoelectronic properties and SEM analysis. A.A., K. Z., and T.D.A. supervised the work. M.-C.T., D.B., R.L., and D.-M.S. assisted with *in situ* GIWAXS measurements. H.D., K.W., S.L., S.D.W., and all the authors contributed to the writing and revisions of the manuscript.

References

- Q. Lin, A. Armin, R. C. R. Nagiri, P. L. Burn and P. Meredith, *Nat Photon*, 2015, **9**, 106-112.
- A. Miyata, A. Mitioglu, P. Plochocka, O. Portugall, J. T.-W. Wang, S. D. Stranks, H. J. Snaith and R. J. Nicholas, *Nat Phys*, 2015, **11**, 582-587.
- F. Hao, C. C. Stoumpos, R. P. Chang and M. G. Kanatzidis, *J. Am. Chem. Soc.*, 2014, **136**, 8094-8099.
- T. Liu, K. Chen, Q. Hu, R. Zhu and Q. Gong, *Adv. Energy Mater.*, 2016, **6**, 1600457.
- V. Gonzalez-Pedro, E. J. Juarez-Perez, W. S. Arsyad, E. M. Barea, F. Fabregat-Santiago, I. Mora-Sero and J. Bisquert, *Nano Lett.*, 2014, **14**, 888-893.
- T. Baikie, Y. Fang, J. M. Kadro, M. Schreyer, F. Wei, S. G. Mhaisalkar, M. Graetzel and T. J. White, *J. Mater. Chem. A*, 2013, **1**, 5628-5641.
- N. R. E. Laboratory, Best Research-Cell Efficiencies Chart, <https://www.nrel.gov/pv/assets/pdfs/best-research-cell-efficiencies-190416.pdf>, (accessed 05 May, 2019).
- M. T. Weller, O. J. Weber, J. M. Frost and A. Walsh, *J. Phys. Chem. Lett.*, 2015, **6**, 3209-3212.
- H. X. Dang, K. Wang, M. Ghasemi, M.-C. Tang, M. De Bastiani, E. Aydin, E. Duzon, D. Barrit, J. Peng, D.-M. Smilgies, S. De Wolf and A. Amassian, *Joule*, 2019, DOI: <https://doi.org/10.1016/j.joule.2019.05.016>.
- N. Pellet, P. Gao, G. Gregori, T. Y. Yang, M. K. Nazeeruddin, J. Maier and M. Gratzel, *Angew. Chem. Int. Ed.*, 2014, **53**, 3151-3157.
- M. Saliba, T. Matsui, J. Y. Seo, K. Domanski, J. P. Correa-Baena, M. K. Nazeeruddin, S. M. Zakeeruddin, W. Tress, A. Abate, A. Hagfeldt and M. Gratzel, *Energy Environ. Sci.*, 2016, **9**, 1989-1997.
- K. Wang, M. C. Tang, H. X. Dang, R. Munir, D. Barrit, M. De Bastiani, E. Aydin, D. M. Smilgies, S. De Wolf and A. Amassian, *Adv Mater*, 2019, **31**, e1808357.
- Y. Deng, Q. Dong, C. Bi, Y. Yuan and J. Huang, *Adv. Energy Mater.*, 2016, **6**, 1600372.
- J. H. Kim, S. T. Williams, N. Cho, C.-C. Chueh and A. K. Y. Jen, *Adv. Energy Mater.*, 2015, **5**, 1401229.
- Z. Yang, C.-C. Chueh, F. Zuo, J. H. Kim, P.-W. Liang and A. K. Y. Jen, *Adv. Energy Mater.*, 2015, **5**, 1500328.
- Y. Deng, E. Peng, Y. Shao, Z. Xiao, Q. Dong and J. Huang, *Energy Environ. Sci.*, 2015, **8**, 1544-1550.
- Y. Deng, Q. Wang, Y. Yuan and J. Huang, *Mater. Horiz.*, 2015, **2**, 578-583.
- K. A. Bush, A. F. Palmstrom, Z. J. Yu, M. Boccard, R. Cheacharoen, J. P. Mailoa, D. P. McMeekin, R. L. Z. Hoyer, C. D. Bailie, T. Leijtens, I. M. Peters, M. C. Minichetti, N. Rolston, R. Prasanna, S. Sofia, D. Harwood, W. Ma, F. Moghadam, H. J. Snaith, T. Buonassisi, Z. C. Holman, S. F. Bent and M. D. McGehee, *Nat. Energy*, 2017, **2**, 17009.
- Y. Zhong, R. Munir, J. Li, M.-C. Tang, M. R. Niazi, D.-M. Smilgies, K. Zhao and A. Amassian, *ACS Energy Lett.*, 2018, **3**, 1078-1085.
- S.-H. Turren-Cruz, M. Saliba, M. T. Mayer, H. Juárez-Santiesteban, X. Mathew, L. Nienhaus, W. Tress, M. P. Erodici, M.-J. Sher, M. G. Bawendi, M. Grätzel, A. Abate, A. Hagfeldt and J.-P. Correa-Baena, *Energy Environ. Sci.*, 2018, **11**, 78-86.
- M. Adnan and J. K. Lee, *Sci. Rep.*, 2018, **8**, 2168.
- P. Fan, D. Gu, G. X. Liang, J. T. Luo, J. L. Chen, Z. H. Zheng and D. P. Zhang, *Sci. Rep.*, 2016, **6**, 29910.
- Z. Li, T. R. Klein, D. H. Kim, M. Yang, J. J. Berry, M. F. A. M. van Hest and K. Zhu, *Nat. Rev. Mater.*, 2018, **3**, 18017.
- M. Park, W. Cho, G. Lee, S. C. Hong, M. C. Kim, J. Yoon, N. Ahn and M. Choi, *Small*, 2019, **15**, e1804005.
- A. J. Huckaba, Y. Lee, R. Xia, S. Paek, V. C. Bassetto, E. Oveisi, A. Lesch, S. Kinge, P. J. Dyson, H. Girault and M. K. Nazeeruddin, *Energy Technol.*, 2019, **7**, 317-324.
- M. Yang, Z. Li, M. O. Reese, O. G. Reid, D. H. Kim, S. Siol, T. R. Klein, Y. Yan, J. J. Berry, M. F. A. M. van Hest and K. Zhu, *Nat. Energy*, 2017, **2**, 17038.
- S. Tang, Y. Deng, X. Zheng, Y. Bai, Y. Fang, Q. Dong, H. Wei and J. Huang, *Adv. Energy Mater.*, 2017, **7**, 1700302.
- J. Sun, J. Wu, X. Tong, F. Lin, Y. Wang and Z. M. Wang, *Adv. Sci.*, 2018, **5**, 1700780.
- J. M. Ball and A. Petrozza, *Nat. Energy*, 2016, **1**, 1-13.

30. Y. Hu, E. M. Hutter, P. Rieder, I. Grill, J. Hanisch, M. F. Aygüler, A. G. Hufnagel, M. Handloser, T. Bein, A. Hartschuh, K. Tvingstedt, V. Dyakonov, A. Baumann, T. J. Savenije, M. L. Petrus and P. Docampo, *Adv. Energy Mater.*, 2018, **8**, 1703057.
31. Q. Hu, L. Zhao, J. Wu, K. Gao, D. Luo, Y. Jiang, Z. Zhang, C. Zhu, E. Schaible, A. Hexemer, C. Wang, Y. Liu, W. Zhang, M. Gratzel, F. Liu, T. P. Russell, R. Zhu and Q. Gong, *Nat. Commun.*, 2017, **8**, 15688.
32. R. Munir, A. D. Sheikh, M. Abdelsamie, H. Hu, L. Yu, K. Zhao, T. Kim, O. E. Tall, R. Li, D. M. Smilgies and A. Amassian, *Adv. Mater.*, 2017, **29**, 1604113.
33. J. Li, R. Munir, Y. Fan, T. Niu, Y. Liu, Y. Zhong, Z. Yang, Y. Tian, B. Liu, J. Sun, D.-M. Smilgies, S. Thoroddsen, A. Amassian, K. Zhao and S. Liu, *Joule*, 2018, **2**, 1313-1330.
34. X. Zhang, R. Munir, Z. Xu, Y. Liu, H. Tsai, W. Nie, J. Li, T. Niu, D.-M. Smilgies, M. G. Kanatzidis, A. D. Mohite, K. Zhao, A. Amassian and S. Liu, *Adv. Mater.*, 2018, **30**, 1707166.
35. G. Giri, R. Li, D. M. Smilgies, E. Q. Li, Y. Diao, K. M. Lenn, M. Chiu, D. W. Lin, R. Allen, J. Reinspach, S. C. Mannsfeld, S. T. Thoroddsen, P. Clancy, Z. Bao and A. Amassian, *Nat. Commun.*, 2014, **5**, 3573.
36. Y. Fan, J. Fang, X. Chang, M.-C. Tang, D. Barrit, Z. Xu, Z. Jiang, J. Wen, H. Zhao, T. Niu, D.-M. Smilgies, S. Jin, Z. Liu, E. Q. Li, A. Amassian, S. Liu and K. Zhao, *Joule*, DOI: 10.1016/j.joule.2019.07.015.
37. P. Gratia, I. Zimmermann, P. Schouwink, J. H. Yum, J. N. Audinot, K. Sivula, T. Wirtz and M. K. Nazeeruddin, *ACS Energy Lett.*, 2017, **2**, 2686-2693.
38. L. S. Ramsdell, *American Mineralogist*, 1947, **32**, 64-82.
39. D. M. Smilgies, R. P. Li, G. Giri, K. W. Chou, Y. Diao, Z. A. Bao and A. Amassian, *Phys Status Solidi-R*, 2013, **7**, 177-179.
40. Y. Zhang, P. Wang, M.-C. Tang, D. Barrit, W. Ke, J. Liu, T. Luo, Y. Liu, T. Niu, D.-M. Smilgies, Z. Yang, Z. Liu, S. Jin, M. G. Kanatzidis, A. Amassian, S. F. Liu and K. Zhao, *J. Am. Chem. Soc.*, 2019, **141**, 2684-2694.
41. D. Barrit, P. Cheng, M.-C. Tang, K. Wang, H. Dang, D.-M. Smilgies, S. F. Liu, T. D. Anthopoulos, K. Zhao and A. Amassian, *Adv. Funct. Mater.*, 2019, **0**, 1807544.
42. T. Niu, J. Lu, M.-C. Tang, D. Barrit, D.-M. Smilgies, Z. Yang, J. Li, Y. Fan, T. Luo, I. McCulloch, A. Amassian, S. Liu and K. Zhao, *Energy Environ. Sci.*, 2018, **11**, 3358-3366.
43. Y. Zhong, R. Munir, A. H. Balawi, A. D. Sheikh, L. Yu, M.-C. Tang, H. Hu, F. Laquai and A. Amassian, *ACS Energy Lett.*, 2016, **1**, 1049-1056.
44. M.-C. Tang, D. Barrit, R. Munir, R. Li, J. M. Barbé, D.-M. Smilgies, S. Del Gobbo, T. D. Anthopoulos and A. Amassian, *Solar RRL*, 2019, **0**.
45. T. Niu, J. Lu, X. Jia, Z. Xu, M. C. Tang, D. Barrit, N. Yuan, J. Ding, X. Zhang, Y. Fan, T. Luo, Y. Zhang, D. M. Smilgies, Z. Liu, A. Amassian, S. Jin, K. Zhao and S. Liu, *Nano Lett.*, 2019, **19**, 7181-7190.
46. Y. Fan, J. Fang, X. Chang, M.-C. Tang, D. Barrit, Z. Xu, Z. Jiang, J. Wen, H. Zhao, T. Niu, D.-M. Smilgies, S. Jin, Z. Liu, E. Q. Li, A. Amassian, S. Liu and K. Zhao, *Joule*, 2019, **3**, 2485-2502.
47. L. A. Perez, K. W. Chou, J. A. Love, T. S. van der Poll, D. M. Smilgies, T. Q. Nguyen, E. J. Kramer, A. Amassian and G. C. Bazan, *Adv. Mater.*, 2013, **25**, 6380-6384.
48. J. L. Baker, L. H. Jimison, S. Mannsfeld, S. Volkman, S. Yin, V. Subramanian, A. Salleo, A. P. Alivisatos and M. F. Toney, *Langmuir*, 2010, **26**, 9146-9151.
49. J. Schlipf and P. Müller-Buschbaum, *Adv. Energy Mater.*, 2017, **7**, 1700131.
50. T. Niu, J. Lu, R. Munir, J. Li, D. Barrit, X. Zhang, H. Hu, Z. Yang, A. Amassian, K. Zhao and S. F. Liu, *Adv. Mater.*, 2018, **30**, e1706576.
51. N. J. Jeon, J. H. Noh, W. S. Yang, Y. C. Kim, S. Ryu, J. Seo and S. I. Seok, *Nature*, 2015, **517**, 476-480.
52. J. A. Steele, H. Yuan, C. Y. X. Tan, M. Keshavarz, C. Steuwe, M. B. J. Roeffaers and J. Hofkens, *ACS Nano*, 2017, **11**, 8072-8083.
53. K. Wang, M. C. Tang, H. X. Dang, R. Munir, D. Barrit, M. De Bastiani, E. Aydin, D. M. Smilgies, S. De Wolf and A. Amassian, *Adv. Mater.*, 2019, **0**, e1808357.
54. A. Sharenko, C. Mackeen, L. Jewell, F. Bridges and M. F. Toney, *Chem Mater*, 2017, **29**, 1315-1320.
55. L.-M. Wu, X.-T. Wu and L. Chen, *Coordination Chemistry Reviews*, 2009, **253**, 2787-2804.
56. J. C. Hamill, J. Schwartz and Y.-L. Loo, *Acs Energy Lett*, 2018, **3**, 92-97.
57. C. Ge, M. Hu, P. Wu, Q. Tan, Z. Chen, Y. Wang, J. Shi and J. Feng, *J. Phys. Chem. C*, 2018, **122**, 15973-15978.
58. Y. Mei, P. J. Diemer, M. R. Niazi, R. K. Hallani, K. Jarolimek, C. S. Day, C. Risko, J. E. Anthony, A. Amassian and O. D. Jurchescu, *PNAS*, 2017, **114**, E6739-E6748.
59. R. H. Bube, *J Appl Phys*, 1962, **33**, 1733-1737.
60. Q. Han, S. H. Bae, P. Sun, Y. T. Hsieh, Y. M. Yang, Y. S. Rim, H. Zhao, Q. Chen, W. Shi, G. Li and Y. Yang, *Adv. Mater.*, 2016, **28**, 2253-2258.
61. M. Saliba, T. Matsui, J. Y. Seo, K. Domanski, J. P. Correa-Baena, M. K. Nazeeruddin, S. M. Zakeeruddin, W. Tress, A. Abate, A. Hagfeldt and M. Gratzel, *Energy Environ. Sci.*, 2016, **9**, 1989-1997.